Journal of Materials Chemistry A

ROYAL SOCIETY OF CHEMISTRY

PAPER

View Article Online
View Journal | View Issue

Cite this: J. Mater. Chem. A, 2024, 12, 25887

Boosted Li_2CO_3 reversible conversion utilizing Cu-doped TiB MBene/graphene for Li–CO_2 batteries†

Tingting Luo,[a] Qiong Peng, *[a] Mengmeng Yang,[a] Haojie Hu,[a] Junfei Ding,[a] Yanli Chen,[a] Xiu Gong, [a] Jingliang Yang,[a] Yunpeng Qu,[a] Zeyou Zhou,[b] Xiaosi Qi *[a] and Zhimei Sun *[c]

Two-dimensional transition metal borides (MBenes), particularly TiB, hold promise as electrocatalysts for CO_2-related reactions. However, their bifunctional catalytic performance for reversible Li_2CO_3 conversion in Li–CO_2 batteries remains inferior to that of Ru-based catalysts. We addressed this issue by introducing tensile strain and doping late transition metal atoms (Mn, Fe, Co, Ni, Cu) into the basal plane of a TiB MBene/graphene heterostructure. Spin-polarized density functional theory (DFT) calculations revealed that the Cu-doped TiB/graphene catalyst ($Cu/Ti_{17}B_{18}/G$) exhibits an ultralow CO_2 reduction and evolution overpotential of 0.66 V, enhancing Li_2CO_3 nucleation and reversible conversion with carbon products. This improvement is attributed to weakened adsorption of O-containing intermediates on the Cu-doped surface, facilitated by the down-shifted d-band center and increased antibonding state occupancy. Consequently, $Cu/Ti_{17}B_{18}/G$ emerges as a promising bifunctional electrocatalyst for Li–CO_2 batteries, outperforming pristine TiB/G and other reported catalysts. Furthermore, its bifunctional activity can be further improved by applying x-direction tensile strain. Molecular dynamics simulations combined with explicit solvent models further confirmed the catalytic durability and stability of $Cu/Ti_{17}B_{18}/G$ in solution. This work provides valuable atomic-scale insights for exploring advanced Li–CO_2 battery catalysts.

Received 31st July 2024
Accepted 2nd September 2024

DOI: 10.1039/d4ta05343e

rsc.li/materials-a

1. Introduction

The aprotic Li–CO_2 battery, owing to its high theoretical energy density of up to 1876 mA h g^{-1} and its CO_2 neutralization capability, is one of the most promising energy storage and conversion technologies.[1–3] The discharge/charge process involves a reversible Li_2CO_3 nucleation/decomposition reaction (*i.e.*, CO_2 reduction/evolution reaction, CO_2RR/CO_2ER), represented by the reaction: $4Li + 3CO_2 \rightleftarrows 2Li_2CO_3 + C$.[4–6] However, the sluggish kinetics and incomplete reactions lead to the accumulation of Li_2CO_3 products and the generation of reactive oxygen species, which can block active sites and diminish battery efficiency.[7–10] Additionally, the inert nature of CO_2 and the wide bandgap of Li_2CO_3 present pronounced activation energy barriers, directly limiting the reversible Li_2CO_3 conversion in Li–CO_2 batteries.[11,12] Therefore, it is desirable yet challenging to develop highly active and stable bifunctional electrocatalysts that not only drive the CO_2 activation but also facilitate the Li_2CO_3 nucleation and reversible decomposition with carbon products.[13–15]

Two-dimensional (2D) orthorhombic transition metal borides (MBenes) have been widely explored as potential catalysts in diverse electrochemical reactions ascribed to their outstanding electrical conductivity and abundance of active sites.[16–19] Among these, titanium boride (TiB) stands out as it has been successfully synthesized and is the lightest MBene, making it highly suitable for portable and lightweight battery applications.[16,20] Notably, Mir *et al.* demonstrated that TiB exhibits stronger adsorption energies compared to VB, CrB, MnB, and FeB, along with excellent electrical conductivity and dynamic stability, making it highly effective for CO_2 capture and activation.[20,21] Our recent research further revealed the inherent catalytic activity of 2D TiB basal plane for converting CO_2 into Li_2CO_3 and carbon products.[22] This activity is facilitated by the bidirectional electron transfer between CO_2 reactants and the TiB surface. Unfortunately, the bifunctional catalytic performance of TiB still lags behind that of noble metal Ru-based catalysts. A significant limitation is the excessive adsorption of Li/C/O intermediates on the TiB plane, which hampers the reversible conversion of Li_2CO_3.

In this study, we aim to overcome these limitations by doping late transition metals (TM = Mn, Fe, Co, Ni, Cu) into the basal plane of TiB MBene and coupling this modified structure with graphene to form a stable heterostructure. The use of late

[a]College of Physics, Guizhou University, Guiyang 550025, China. E-mail: qpeng@gzu.edu.cn; xsqi@gzu.edu.cn

[b]State Grid Fujian Electric Power Research Institute, Fuzhou 350007, China

[c]School of Materials Science and Engineering, Beihang University, Beijing 100191, China. E-mail: zmsun@buaa.edu.cn

† Electronic supplementary information (ESI) available. See DOI: https://doi.org/10.1039/d4ta05343e

transition metals with paired d electrons can facilitate electron compensation with the empty or unpaired d orbitals of Ti atoms in the TiB plane, which is expected to balance the adsorption strength of intermediates on the catalytic surface.[22] In addition, among the catalysts studied so far, Cu remains the only heterogeneous electrocatalyst for selective CO_2 electroreduction to multicarbon (C_{2+}) products.[23,24] Therefore, doping with late transition metals, particularly Cu, which has fully paired d-electrons, is anticipated to reshape the electronic structure of TiB and alleviate the excessive adsorption of Li/C/O intermediates on the TiB plane. Using spin-polarized density functional theory (DFT) calculations, we first investigate the stability of late transition metals-doped TiB/graphene heterostructures (TM/$Ti_{17}B_{18}$/G, TM = Mn, Fe, Co, Ni, Cu). Subsequently, we explore the electrochemical reaction mechanisms in Li–CO_2 batteries. Notably, the Cu/$Ti_{17}B_{18}$/G catalyst delivers optimal bifunctional catalytic activity for Li_2CO_3 nucleation and reversible conversion, achieving an ultralow overpotential of 0.66 V. Furthermore, tensile strain is applied to tailor the d-band center and enhance the bifunctional activity of the catalyst. Finally, molecular dynamics simulations are conducted to assess the catalytic durability of the Cu/$Ti_{17}B_{18}$/G heterostructure in solution. This research provides valuable insights into the atomic-level interactions and mechanisms that drive the improved Li_2CO_3 reversible conversion performance of Cu-doped TiB MBene/graphene electrocatalysts, paving the way for the development of advanced multifunctional catalysts for next-generation Li–CO_2 batteries.

2. Computational methods and models

Utilizing the Vienna *Ab initio* Simulation Package (VASP),[25–27] spin-polarized density functional theory (DFT) calculations were conducted to investigate the structural stability and electrocatalytic properties. The ALKEMIE[28] and VASPKIT[29] codes were implemented to postprocess the computational data. The PBE-D3 exchange–correlation[30] was chosen to elucidate the interaction dynamics between reaction intermediates and catalytic active sites.[31] The plane wave cut-off energy was set at 500 eV. All configurations were based on a 4 × 4 supercell of graphene and 3 × 3 supercell of TiB with a vacuum slab of 25 Å inserted in the z direction to prevent interaction between two neighboring surfaces. Crystal orbital Hamilton population (COHP) analyses were performed using the LOBSTER package.[32] Furthermore, the Bader charge analysis was applied to quantify the charge transfer.[33,34] To capture each saddle-point structure and the associated minimum energy path during the oxidative dissociation of Li_2CO_3, climbing image nudged elastic band (CINEB) calculations were performed.[35] *Ab initio* molecular dynamics (AIMD) simulations were conducted to assess the thermodynamic stability under reaction conditions at 300 K for a duration of 10 ps, with a time step of 2 fs.[36] In this simulation, tetraethylene glycol dimethyl ether (TEGDME, $CH_3O(CH_2CH_2O)_4CH_3$), with a density of 1.007 g cm^{-3} and low dielectric permittivity of 7.79,[37] was utilized as the organic solvation medium.[38] The radial distribution function $g(r)$ and the coordination number[39] were obtained using the VASPKIT code.

The TiB/G heterostructure consists of 18 Ti atoms, 18 B atoms, and 32 C atoms; the lattice parameters of TiB and graphene are outlined in Table S1 of (ESI).† Subsequently, a single Ti atom was removed from TiB/G to anchor a late transition metal (TM) atom, such as Mn, Fe, Co, Ni and Cu. The thermodynamic stability of TM/$Ti_{17}B_{18}$/G systems was confirmed by the negative formation energy (E_f) (Table S2†), which was calculated using the following equation:

$$E_f = E_{TM/Ti_{17}B_{18}/G} - E_{Ti_{17}B_{18}/G} - E_{TM}^{bulk} \quad (1)$$

where $E_{TM/Ti_{17}B_{18}/G}$ and $E_{Ti_{17}B_{18}/G}$ denote the energies of TM/$Ti_{17}B_{18}$/G composite and $Ti_{17}B_{18}$/G substrate, respectively, and E_{TM}^{bulk} represents the total energy of the bulk metal. Additionally, the electrochemical stability of the TM/$Ti_{17}B_{18}$/G catalysts was evaluated using the following formula:

$$U_{diss} = U_{diss}^0 - E_b/N_e \quad (2)$$

where U_{diss}^0 and N_e refer to the standard electrode potential of bulk metal and the number of electrons transferred in the dissolution process, respectively. As shown in Table S3,† the U_{diss} is greater than 0 V (*vs.* SHE), indicating that the considered TM/$Ti_{17}B_{18}$/G catalysts are electrochemically stable. The E_b represents the binding energy obtained from the following equation:

$$E_b = E_{TM/Ti_{17}B_{18}/G} - E_{Ti_{17}B_{18}/G} - E_{TM}^{isolated} \quad (3)$$

where $E_{TM}^{isolated}$ is the energy of an isolated transition metal. A more negative E_b value denotes stronger adsorption of the metal atom on the defective TiB/G substrate. In addition, the stress–strain and energy–strain methodologies were employed to investigate the mechanical properties.[40–43] When a uniaxial stress was imposed in the x or y directions, the strain was defined as:

$$\varepsilon = \frac{a - a_0}{a_0} \times 100\% \quad (4)$$

here, a and a_0 signify the lattice constants of the strained and unstrained systems.

To monitor the reaction process on different catalysts, the Gibbs free energies of Li–CO_2 reaction intermediates were calculated using eqn (5).[44] Particularly, in the Li–CO_2 batteries, $Li^+ + e^- \rightleftarrows$ Li is in equilibrium with bulk Li at 0 V.

$$\Delta G = \Delta E_{DFT} + \Delta E_{ZPE} - T\Delta S + neU \quad (5)$$

where ΔE_{DFT}, ΔE_{ZPE} and ΔS are the DFT total energy difference, zero-point energy change, and entropy change at T = 298.15 K, respectively, which are given in Tables S4–S6.† The term U stands for the applied electrode potential, and n represents the number of transferred electrons. For the Li–CO_2 battery, the discharge potential (U_{DC}) during CO_2RR and charge potential (U_C) during CO_2ER correspond to the minimum/maximum potentials required to sustain the redox processes. The

deviation between the discharge/charge potential and theoretical equilibrium potential (U_{eq} = 2.87 V) signifies the CO_2RR/CO_2ER overpotentials, *i.e.*, $\eta_{CO_2RR} = U_{eq} - U_{DC}$ and $\eta_{CO_2ER} = U_C - U_{eq}$. Herein, we applied the total overpotentials for CO_2RR and CO_2ER ($\eta_{tot} = \eta_{CO_2RR} + \eta_{CO_2ER}$) as a quantitative metric to assess the bifunctional activity of targeted catalysts for Li–CO_2 redox.

3. Results and discussion

3.1. Insight into TiB MBene material design

Fig. 1a presents the material design idea of late transition metal Cu doped TiB MBene/graphene heterostructure to alleviate the adsorption strength of Li/C/O intermediates. Taking advantage of the unique electronic configuration of late transition metals, Cu dopant is expected to serve as a d-electron buffer. Moreover, the maximum lattice mismatch between TiB with 3 × 3 supercell and graphene with $2\sqrt{3} \times 4$ supercell was found to be 4.18%, demonstrating they are good counterparts for establishing high-quality heterostructures. The negative formation energy in Fig. 1b signifies the thermodynamical stability of transition metals Mn, Fe, Co, Ni, Cu doped TiB/graphene heterostructures (TM/$Ti_{17}B_{18}$/G). As demonstrated by Jang *et al.*,[45] sp^2 hybridized graphene can capture electrons from the metal layer, resulting in strong interface coupling that stabilizes the metal catalyst and modifies its electronic properties. Indeed, there are abundant electrons localized at the Cu/$Ti_{17}B_{18}$/G heterointerface, and graphene capture 3.46 electrons from the Cu/$Ti_{17}B_{18}$ layer (Fig. S1†), suggesting a strong coupling between them. The Cu dopant exhibits a lower d-band center (ε_d) of −2.78 eV in comparison with pristine TiB/G (ε_d = −2.55 eV). According to the d-band center theory,[46–48] the down-shifted ε_d signifies a weakened binding capability of the active site for reaction intermediates. Therefore, a lower d-band center in Cu/$Ti_{17}B_{18}$/G holds promise for alleviating the intense intermediate adsorption issue on the pristine TiB surface. Next, we will confirm this idea using the spin-polarized DFT calculations and constant potential solvation models in ESI.†

3.2. Reaction mechanism and electrocatalytic performance

Promising bifunctional catalysts should strike a balance between the CO_2 reduction and evolution, *i.e.*, Li_2CO_3 generation and its reversible dissociation. Fig. S2† lists several possible pathways for CO_2 reduction to $Li_2C_2O_4$ and Li_2CO_3 during the initial $2e^-$ step of the discharging process. Prior studies have shown that the nucleation selectivity of Li_2CO_3 and $Li_2C_2O_4$ is dependent on the applied catalysts.[5,49] For each reaction intermediate, distinct adsorption configurations are taken into account in Fig. S3† and the energetically optimal one is displayed in Fig. 2a. Worth noting that the $*Li_2C_2O_4$ nucleation is not as stable as that of $*Li_2CO_3$ on both TiB/G and Cu/$Ti_{17}B_{18}$/G surfaces, which is prone to decompose into $*Li_2CO_3$ and *CO, regardless of the specific CO_2 reduction pathway. This disproportionation splitting is energetically favorable, with an exothermic free energy change of −1.25 eV on TiB/G surface and −2.21 eV on Cu/$Ti_{17}B_{18}$/G surface. Thus, $*Li_2CO_3$ is identified as the final discharge product for TiB/G and Cu/$Ti_{17}B_{18}$/G use in Li–CO_2 batteries, analogue to Ru(0001) catalyst.[50] Generally, a catalyst with Li_2CO_3 nucleation selectivity is promising for achieving efficient four-electron ($4e^-$) CO_2 reduction ($4Li^+ + 3CO_2 + 4e^- \rightarrow 2Li_2CO_3 + C$) in Li–$CO_2$ batteries.[51,52]

For the reverse CO_2 evolution process, the dissociation of Li_2CO_3 and the participation of amorphous carbon products play

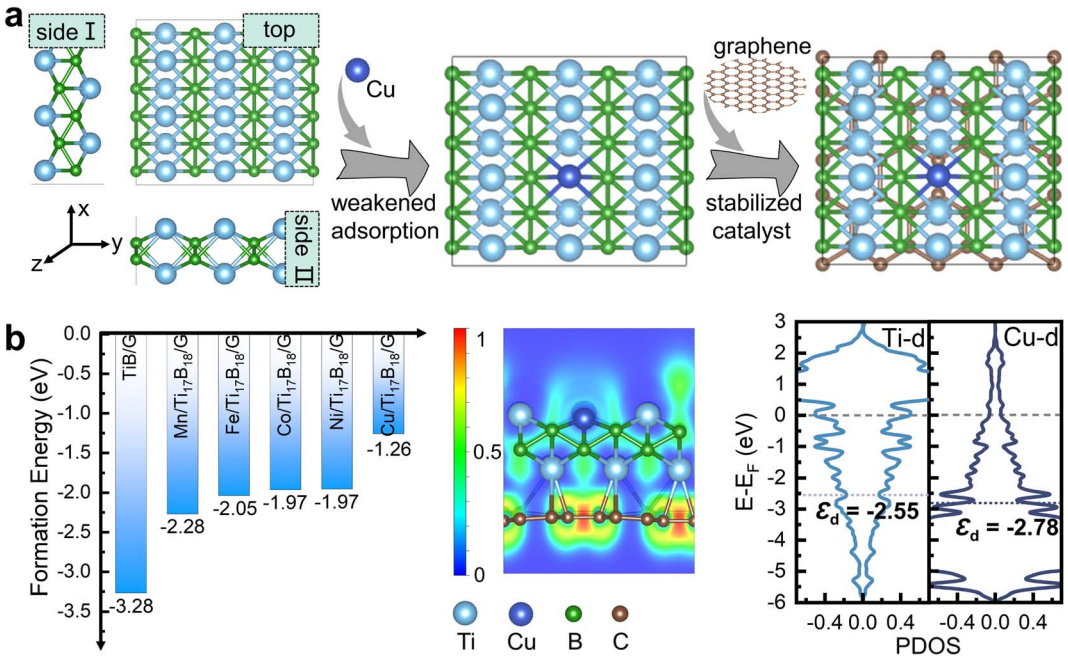

Fig. 1 (a) Schematic of the TiB MBene/graphene heterostructure design. (b) Formation energy of late transition metal atoms (Mn, Fe, Co, Ni, Cu) doped TiB/G heterostructure and electronic properties of Cu/$Ti_{17}B_{18}$/G.

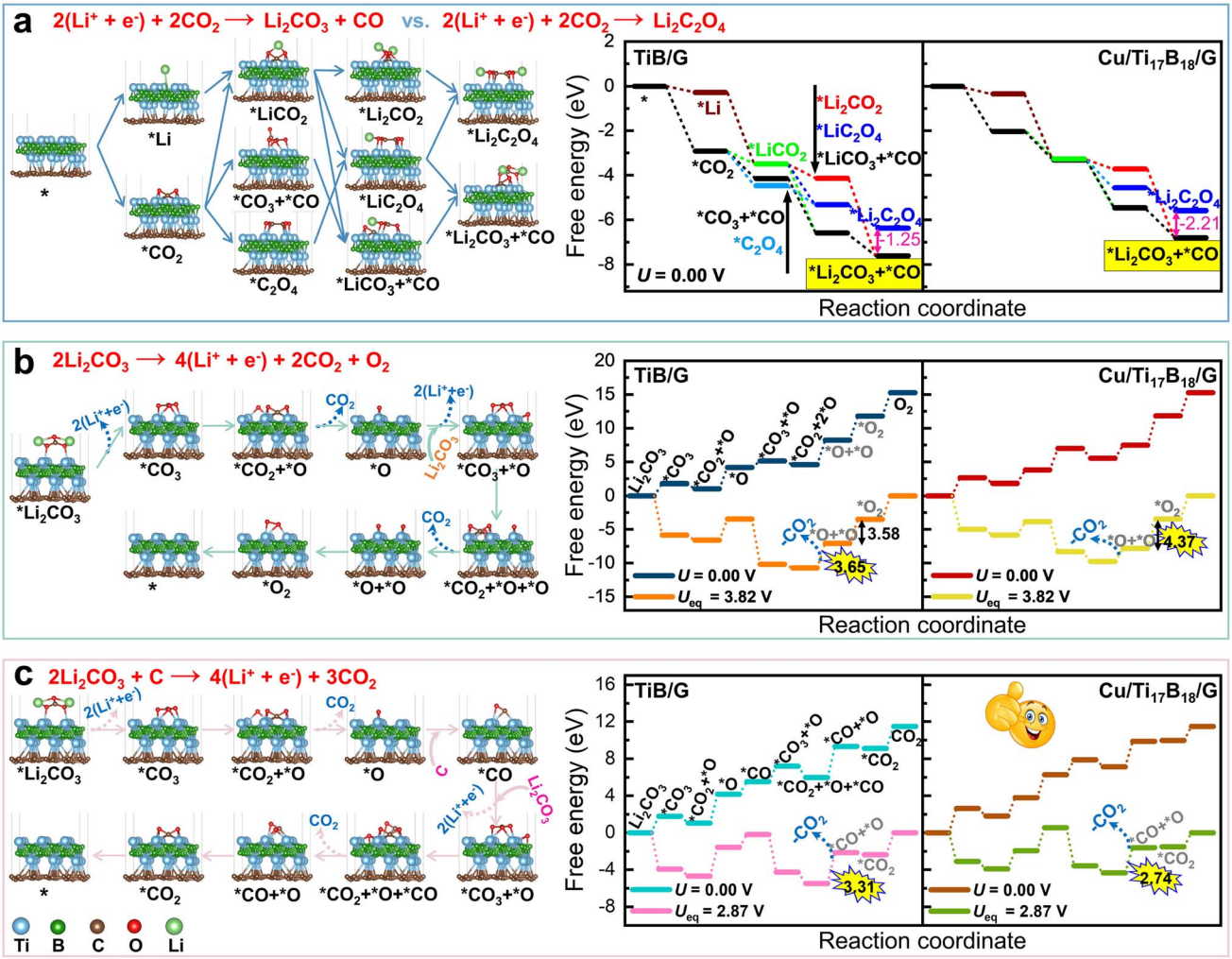

Fig. 2 (a) Nucleation selectivity of $*Li_2C_2O_4$ and $*Li_2CO_3$ on pristine and Cu-doped TiB/G catalysts. (b) Self-decomposition of Li_2CO_3 to evolve O_2. (c) The co-decomposition of Li_2CO_3 and carbon to regenerate original reactants, where the rate-determining step is highlighted.

a decisive role in the cycling stability of Li–CO_2 batteries.[53] If amorphous carbon is not involved in the Li_2CO_3 decomposition, aggressive oxygen species will be generated and accumulated, passivating the electrocatalysts.[54] As depicted in Fig. S4,† Cu/$Ti_{17}B_{18}$/G exhibits a much lower energy barrier (1.09 eV) for Li_2CO_3 decomposition, in comparison with that of graphene-based single-atom catalyst Cr@G (1.67 eV), single-layer MoS_2 (2.63 eV), and ReS_2 (2.36 eV) catalysts.[55,56] The free energy changes associated with the self-decomposition of Li_2CO_3 or its co-oxidative dissociation with carbon products are graphically illustrated in Fig. 2b and c. Evidently, when carbon products engage in the Li_2CO_3 decomposition through the oxidative reaction $2Li_2CO_3 + C \rightarrow 4Li^+ + 3CO_2 + 4e^-$, the Cu/$Ti_{17}B_{18}$/G catalyst presents the lowest rate-determining step (RDS) energy barrier of 2.74 eV. These findings indicate that the Cu/$Ti_{17}B_{18}$/G catalyst possesses the dual capability of facilitating the selective Li_2CO_3 nucleation and efficiently promoting its reversible dissociation to original reactants, meriting further exploration.

Therefore, to assess the bifunctional CO_2RR/CO_2ER activity of TiB/G and Cu/$Ti_{17}B_{18}$/G in Li–CO_2 batteries, a continuous four-electron transfer mechanism is adopted in Fig. 3a. During the initial $2e^-$ step of the discharge process, CO_2 and Li^+ are co-adsorbed on the catalyst surface to yield $*LiCO_2$ intermediate, which then reacts with additional Li^+ and CO_2 to form the first Li_2CO_3 product and *CO intermediate. In the subsequent $2e^-$ step, the *CO further reacts with two Li^+ and one CO_2 molecule to produce the second Li_2CO_3 and amorphous C.[13] As seen in Fig. S5,† the CO_2RR/CO_2ER overpotential of TiB/G reaches 2.43 V. During discharging, the potential-determining step (PDS) corresponds to the third electron transfer step (*i.e.*, the formation of carbon products), while the PDS during charging is the Li_2CO_3 decomposition on TiB/G surface. Notably, the introduction of Cu into the TiB/G plane effectively balances the adsorption and desorption of $Li_xC_yO_z$ ($x = 0$–2, $y = 1$–2, $z = 1$–3) reaction intermediates, leading to a shift in the PDS from the latter $2e^-$ transfer step to the initial $2e^-$ steps. Of greater interest is that the Cu/$Ti_{17}B_{18}$/G catalyst delivers a dramatically decreased CO_2RR/CO_2ER overpotential as low as 0.66 V (Fig. 3b). Fig. 3c summarizes the overpotentials of other excellent Li–CO_2 battery electrode catalysts. This performance

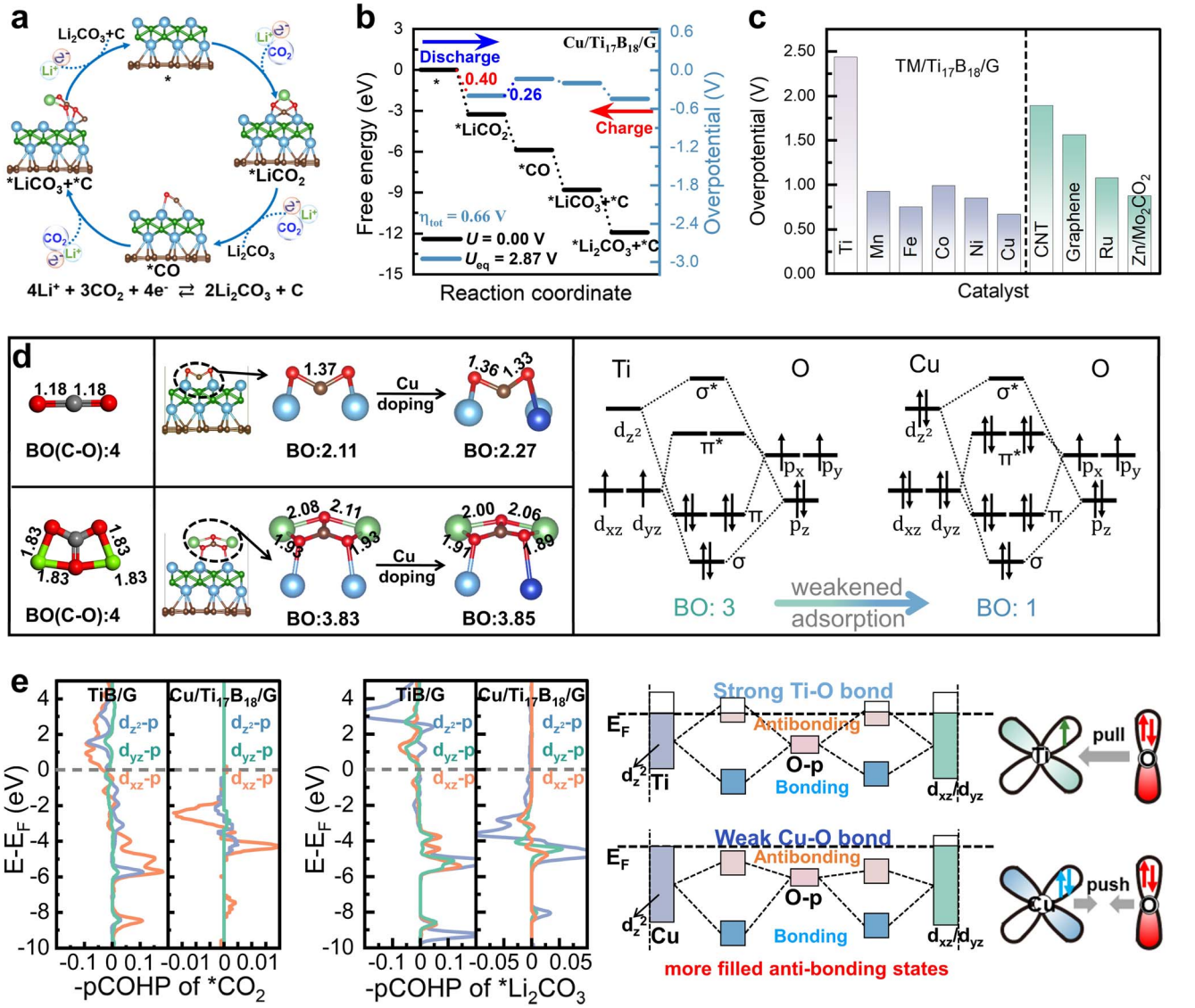

Fig. 3 (a) Continuous four-electron transfer pathway. (b) Free energy diagrams for $Cu/Ti_{17}B_{18}/G$, where blue and red numbers represent CO_2RR overpotential (η_{CO_2RR}) during discharge and CO_2ER overpotential (η_{CO_2ER}) during charge, respectively, and η_{tot} represents the total overpotential. (c) Comparation of total overpotential with available references. (d) Cu as a dopant reducing bond order (BO) in CO_2 and Li_2CO_3 adsorbates. (e) Evolutions of bonding and antibonding states in p–d orbital interactions, where the spin-up and spin-down channels are identical in the projected crystal orbital Hamilton population (pCOHP) due to the zero magnetic moment of the system.

surpasses that of pristine TiB/G and previously reported carbon nanotubes (1.94 V), graphene (1.56 V),[57,58] noble metal Ru (1.07 V)[50] and single-atom modified MXenes like Zn/Mo_2CO_2 (0.97 V).[13] Besides, Fig. S6† depicts their Gibbs free energy for Li–CO_2 electrochemistry *via* a continuous $4e^-$ transfer pathway for other late transition metal modified TiB/G catalysts such as Mn, Fe, Co, and Ni. Remarkably, compared to pristine TiB/G (η_{tot} = 2.43 V), the obtained $Mn/Ti_{17}B_{18}/G$, $Fe/Ti_{17}B_{18}/G$, $Co/Ti_{17}B_{18}/G$, and $Ni/Ti_{17}B_{18}/G$ catalysts exhibit dramatically narrowed CO_2RR/CO_2ER overpotential as low as 0.92, 0.75, 0.99 and 0.84 V. This validates that doping engineering can be used as a guideline for the rational design of bifunctional electrocatalysts aimed at achieving reversible CO_2 and Li_2CO_3 conversion in Li–CO_2 batteries.

Given the pivotal role of CO_2 and Li_2CO_3 as reactants and products in Li–CO_2 batteries, we further explored the intricate relationship between p- and d-electron interactions and bifunctional activity at the atomic orbital level by focusing on their adsorption on TiB/G and $Cu/Ti_{17}B_{18}/G$ surfaces. A striking similarity emerges: CO_2 and Li_2CO_3 are adsorbed *via* O p orbitals interacting with Ti or Cu d orbitals. As seen in Fig. S7,† there are three possible modes of p–d orbital interactions based on the principle of maximum overlap.[59] Specifically, the metal d_{z^2} orbitals hybridize with the O p_z orbitals to form σ bonds, whereas the d_{xz}/d_{yz} orbitals hybridize with p_x/p_y to form π bonds (Fig. 3d).[60] It is seen that the d_{z^2}, d_{xz} and d_{yz} electrons of Ti are occupied near the Fermi level (Fig. S8†), triggering the donation of d-electrons to the empty CO_2 antibonding orbitals,

yielding robust Ti–O bonding and excessive intermediate adsorption on the TiB/G plane. In sharp contrast, Cu d electrons are almost concentrated below the Fermi level (Fig. S9†) with a lower d-band center than Ti, yielding weakened interactions with O-containing intermediates. Further analysis of the projected crystal orbital Hamilton population (pCOHP) in Fig. 3e reveals that the orbital interactions between Cu d orbitals and O p orbitals induce more filled antibonding states below the Fermi level, indicating a weakened Cu–O bonding. Analogous trends are observed in the case of Li_2CO_3 adsorption. The reduced d-band center and increased antibonding state occupancy highlight the role of Cu dopants in mitigating the strong $Li_xC_yO_z$ adsorption on TiB/G. Therefore, the Cu/$Ti_{17}B_{18}$/G catalyst achieves enhanced bifunctional activity for the CO_2 reduction to Li_2CO_3 and its reversible conversion with carbon products.

3.3. Strain effects

We continue investigated the bifunctional catalytic performance of TiB/G and Cu/$Ti_{17}B_{18}$/G for Li_2CO_3 reversible conversion under uniaxial strain with a magnitude from −4% to +4%. The uniaxial stress–strain curves in Fig. S10a† illustrate that these TiB/G and Cu/$Ti_{17}B_{18}$/G materials can endure ultimate tensile strains of up to 22% and 26% along the *x*-direction, respectively, while withstanding up to 22% along the *y*-direction, delivering superior mechanical flexibility comparable to graphene. Furthermore, the differences in Young's modulus between the *x*- and *y*-directions (Fig. S10b†) highlight the anisotropic mechanical properties of TiB/G and Cu/$Ti_{17}B_{18}$/G.

Unlike transition metal doping, which significantly alters the PDS, applying uniaxial strain in the *x*-direction hardly changes the PDS for a given catalyst. As shown in Fig. S11 and S12,† the PDS during the discharge–charge process for TiB/G is almost maintained at the latter $2e^-$ transfer step under *x*-direction strain ranging from −4% to +4%, while the PDS for Cu/$Ti_{17}B_{18}$/G remains at the initial $2e^-$ transfer step. This indicates that the primary effect of *x*-direction strain is to lower the energy barrier of the PDS, rather than altering the PDS itself. This explains why the increase of d-band center under *x*-direction strain, which signifies stronger interactions with reaction intermediates,[61] results in a decrease in overpotential of the catalyst (Fig. 4a). Consequently, the overpotential for TiB/G decreases from 2.00 V to 1.83 V as strain varies from −4% to +4%, and for Cu/$Ti_{17}B_{18}$/G, it decreases from 0.72 V to 0.45 V. Similar enhancement of catalytic activity by strain engineering has been observed in other studies.[62,63]

In contrast, *y*-direction strain induces minimal changes in the d-band center, leading to a less significant impact on overpotential, as shown in Fig. 4b. The different strain effects in the *x*- and *y*-directions on overpotentials are due to the anisotropic mechanical properties of TiB/G and Cu/$Ti_{17}B_{18}$/G. As shown in Table S7† for TiB/G, the Young's modulus in the *y*-direction (562.5 N m^{-1}) is approximately 1.3 times higher than in the *x*-direction (431.6 N m^{-1}), which is much higher than that of isotropic materials like graphene (342 N m^{-1}) and MoS_2 (130 N m^{-1}).[64] This mechanical anisotropy, coupled with the ultrahigh Young's modulus, results in the relatively stable d-band center and overpotential for TiB/G and Cu/$Ti_{17}B_{18}$/G

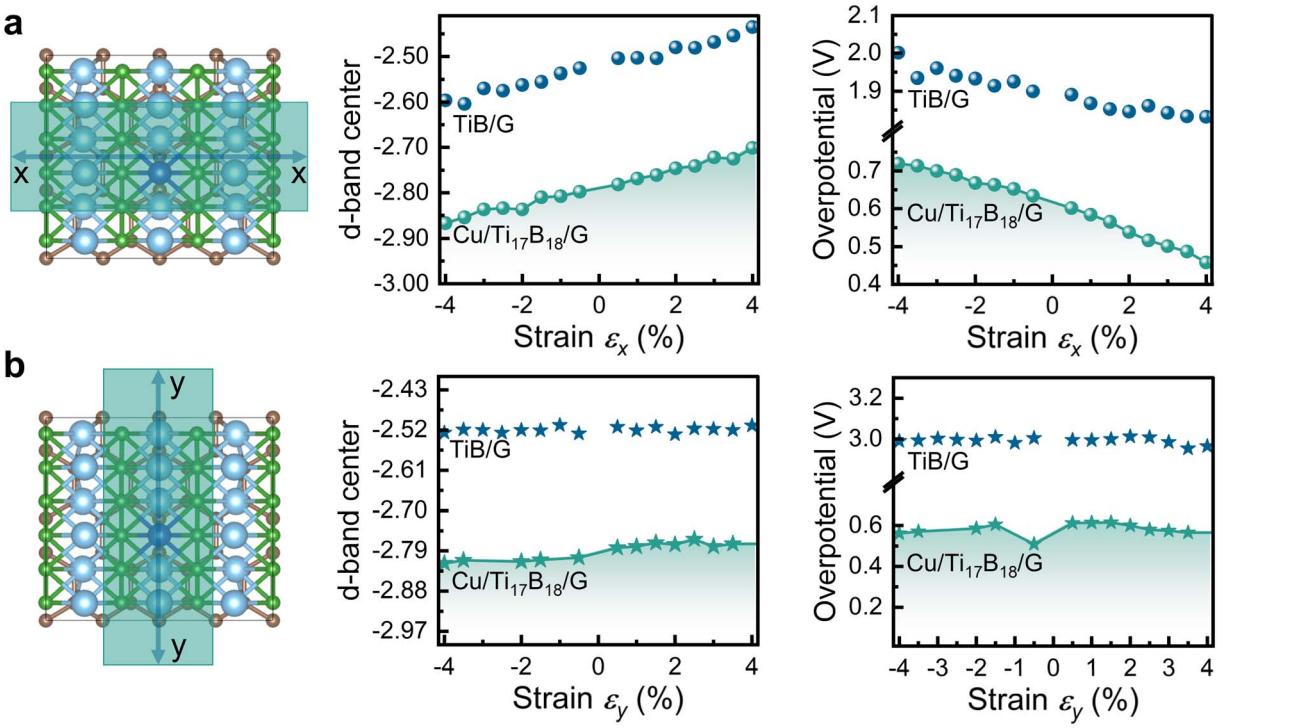

Fig. 4 The d-band centers (ε_d) shifts and overpotentials of TiB/G and Cu/$Ti_{17}B_{18}$/G under (a) *x*-direction and (b) *y*-direction strains with a magnitude from −4% to +4%.

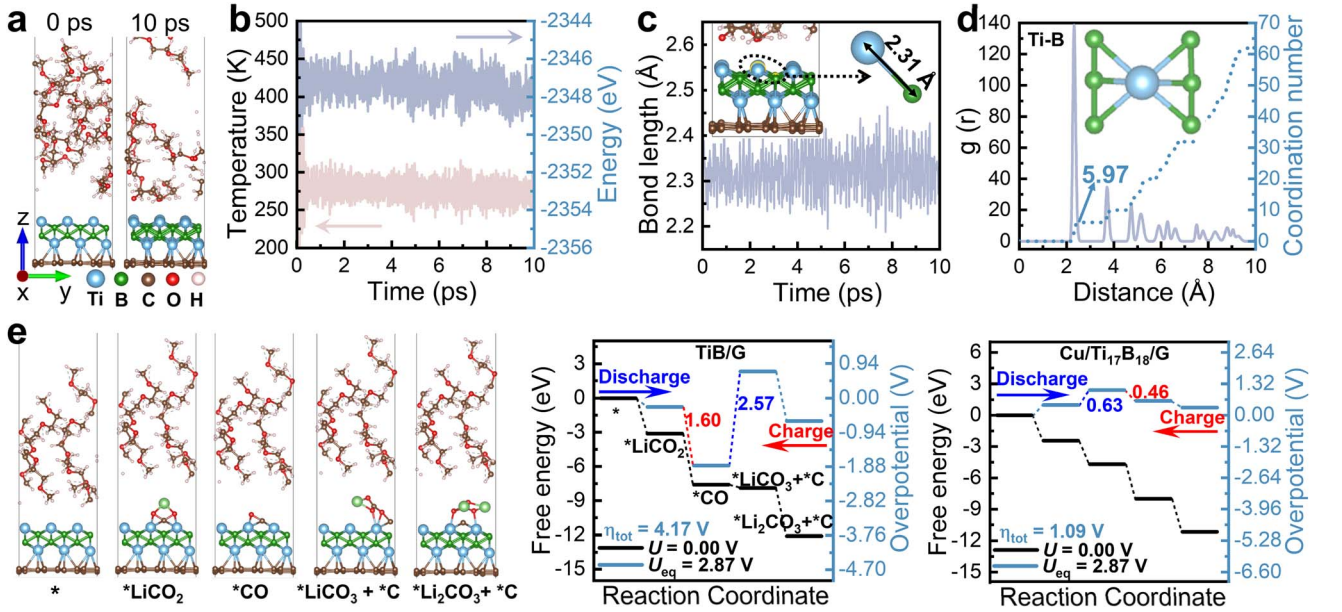

Fig. 5 (a–d) Evolutions of TiB/G structure, temperature and energy, Ti–B bond length, radial distribution function $g(r)$ and coordination number during AIMD simulations at 300 K. (e) Optimized intermediates and free energy diagrams under the explicit TEGDME solvent environment.

under external y-axial strains. Overall, direction-specific strain engineering, along with metal doping, proves to be an effective strategy for enhancing the bifunctional catalytic properties of TiB-based materials in Li–CO_2 batteries.

3.4. Stability in solution

To evaluate the durability of catalysts in an organic solvation medium, we assessed the thermal stability of TiB/G in a TEGDME solution at 300 K for 10 ps using AIMD simulations. TEGDME delivers flexible linear chain structure, low viscosity, and moderate dielectric constant (7.79) to enhance Li-ion mobility, making it an ideal solvent for Li–CO_2 batteries.[65,66] As shown in Fig. 5a, after 10 ps, the final TiB/G structure remained intact, with no bond breakage or structural rearrangement. Additionally, both temperature and total energy fluctuations were minimal, remaining within a narrow range (Fig. 5b). The Ti–B bond length maintained consistent at approximately 2.31 Å throughout the AIMD process (Fig. 5c). The radial distribution function $g(r)$, presented in Fig. 5d, indicates that the TiB/G heterostructure maintained excellent crystallization post-annealing, with Ti atoms predominantly coordinated by B atoms, and an average coordination number of approximately 5.97. These findings confirm that the TiB/G catalyst structure is robustly stable in the solution. Notably, the explicit solvent model depicted in Fig. 5e demonstrates that Cu doping significantly reduces the overpotential for Li_2CO_3 reversible conversion to 1.09 V, compared to 4.17 V for pristine TiB/G as Li–CO_2 battery catalyst.

The potential influence of other solvents, such as ethylene carbonate (EC) also examined. EC has a rigid cyclic structure, a high dielectric constant (approximately 90), and higher viscosity compared to TEGDME, which leads to strong interactions with lithium ions.[67] As shown in Fig. S13,† the AIMD results demonstrate that due to the presence of a carbon–oxygen ring with an ester linkage in EC molecules, EC strongly interacts with TiB/G over time, making EC unsuitable as a solvent for TiB-based catalysts in Li–CO_2 batteries. To provide a more solid reference to the experiments, the constant potential implicit solvent model[68,69] is employed to investigate the catalytic selectivity and bifunctional activity of both pristine and Cu-doped TiB/G catalysts (see ESI†).

4. Conclusions

In summary, we uncovered the origins of the enhanced activity of Cu-doped TiB MBene/graphene heterostructure in Li–CO_2 electrochemistry. By incorporating late transition metals with paired d electrons into the TiB/G structure, we achieved significantly improved bifunctional activity for the reversible conversion of Li_2CO_3. Specifically, the Cu/$Ti_{17}B_{18}$/G catalyst demonstrated an ultralow overpotential of 0.66 V for both CO_2 reduction and evolution reactions. This enhancement is attributed to the down-shifted d-band center and increased antibonding state occupancy in the d_{z^2}–p_z, d_{xz}–p_x and d_{yz}–p_y orbital hybridizations, which mitigates excessive intermediate adsorption on the TiB plane. Remarkably, applying tensile strain along the x-direction to the catalyst not only elevates its d-band center but also lowers the CO_2RR/CO_2ER overpotential, further boosting the bifunctional activity of Cu/$Ti_{17}B_{18}$/G for Li_2CO_3 conversion. Finally, AIMD simulations combined with explicit solvent models confirmed that these catalysts exhibit excellent electrochemical stability and durability in a practical solvent environment. This research highlights the critical role of tuning electronic structures through doping and strain engineering in the design of advanced catalysts, with potential applications across diverse fields.

Data availability

The data supporting this article have been included as part of the ESI.† Raw data is available by contacting the corresponding author.

Author contributions

Tingting Luo, Qiong Peng, Mengmeng Yang and Haojie Hu: conceptualization, investigation, visualization, methodology, writing – original draft. Junfei Ding, Yanli Chen and Xiu Gong: data curation, formal analysis, visualization. Jing-Liang Yang, Yunpeng Qu and Zeyou Zhou: supervision, writing – review & editing. Xiaosi Qi and Zhimei Sun: supervision, funding acquisition, resources, software. All authors contributed to the whole study.

Conflicts of interest

The authors declare no conflict of interest.

Acknowledgements

This work was financially supported by the National Natural Science Foundation of China (No. 52101010, 22005071 and 11964006), Natural Science Special (Special Post) Research Foundation of Guizhou University (No. 2020-020), Platform of Science and Technology and Talent Team Plan of Guizhou province (No. GCC[2023]007), Fok Ying Tung Education Foundation, Major Research Project of innovative Group of Guizhou province (No. 2018-013), Natural Science Foundation of Guizhou province [No. ZK 2022-044].

References

1 Y. Liu, P. Shu, M. Zhang, B. Chen, Y. Song, B. Lu, R. Mao, Q. Peng, G. Zhou and H.-M. Cheng, *ACS Energy Lett.*, 2024, **9**, 2173–2181.
2 D. Wang, J. Yang, P. He and H. Zhou, *Energy Environ. Sci.*, 2021, **14**, 4107–4114.
3 J. Lin, J. Ding, H. Wang, X. Yang, X. Zheng, Z. Huang, W. Song, J. Ding, X. Han and W. Hu, *Adv. Mater.*, 2022, **34**, 2200559.
4 J. Chen, X.-Y. Chen, Y. Liu, Y. Qiao, S.-Y. Guan, L. Li and S.-L. Chou, *Energy Environ. Sci.*, 2023, **16**, 792–829.
5 Y. Yang, K. Guo, D. Yuan, J. Cheng and B. Wang, *J. Am. Chem. Soc.*, 2020, **142**, 6983–6990.
6 Y. Wang, J. Zhou, C. Lin, B. Chen, Z. Guan, A. M. Ebrahim, G. Qian, C. Ye, L. Chen, Y. Ge, Q. Yun, X. Wang, X. Zhou, G. Wang, K. Li, P. Lu, Y. Ma, Y. Xiong, T. Wang, L. Zheng, S. Chu, Y. Chen, B. Wang, C.-S. Lee, Y. Liu, Q. Zhang and Z. Fan, *Adv. Funct. Mater.*, 2022, **32**, 2202737.
7 X. Zhang, Y. Wang and Y. Li, *J. Phys. Chem. Lett.*, 2023, **14**, 1604–1608.
8 X. Xiao, Z. J. Zhang and P. Tan, *Proc. Natl. Acad. Sci. U. S. A.*, 2023, **120**, e2217454120.
9 S. Chen, K. Yang, H. Zhu, J. Wang, Y. Gong, H. Li, M. Wang, W. Zhao, Y. Ji, F. Pan, S. R. P. Silva, Y. Zhao and L. Yang, *Nano Energy*, 2023, **117**, 108872.
10 J. Zhou, T. Wang, L. Chen, L. Liao, Y. Wang, S. Xi, B. Chen, T. Lin, Q. Zhang, C. Ye, X. Zhou, Z. Guan, L. Zhai, Z. He, G. Wang, J. Wang, J. Yu, Y. Ma, P. Lu, Y. Xiong, S. Lu, Y. Chen, B. Wang, C. S. Lee, J. Cheng, L. Gu, T. Zhao and Z. Fan, *Proc. Natl. Acad. Sci. U. S. A.*, 2022, **119**, e2204666119.
11 R. Huang, Z. Zhai, X. Chen, Q. Liu, H. Yu, B. Li and S. Yin, *Chem. Eng. J.*, 2024, **489**, 151191.
12 J. Xie, Z. Zhou and Y. Wang, *Adv. Funct. Mater.*, 2020, **30**, 1908285.
13 Y. Shi, B. Wei, D. Legut, S. Du, J. S. Francisco and R. Zhang, *Adv. Funct. Mater.*, 2022, **32**, 2210218.
14 B. Lu, X. Wu, X. Xiao, B. Chen, W. Zeng, Y. Liu, Z. Lao, X.-X. Zeng, G. Zhou and J. Yang, *Adv. Mater.*, 2024, **36**, 2308889.
15 J. Zhou, X. Li, C. Yang, Y. Li, K. Guo, J. Cheng, D. Yuan, C. Song, J. Lu and B. Wang, *Adv. Mater.*, 2019, **31**, 1804439.
16 T. Xu, Y. Wang, Z. Xiong, Y. Wang, Y. Zhou and X. Li, *Nano-Micro Lett.*, 2023, **15**, 6.
17 X. Bai, Z. Zhao and G. Lu, *J. Phys. Chem. Lett.*, 2023, **14**, 5172–5180.
18 T. Zhang, B. Zhang, Q. Peng, J. Zhou and Z. Sun, *J. Mater. Chem. A*, 2021, **9**, 433–441.
19 M. Zafari, A. S. Nissimagoudar, M. Umer, G. Lee and K. S. Kim, *J. Mater. Chem. A*, 2021, **9**, 9203–9213.
20 S. H. Mir, V. K. Yadav and J. K. Singh, *ACS Appl. Mater. Interfaces*, 2022, **14**, 29703–29710.
21 M. Ozkan, K. A. M. Quiros, J. M. Watkins, T. M. Nelson, N. D. Singh, M. Chowdhury, T. Namboodiri, K. R. Talluri and E. Yuan, *Chem*, 2024, **10**, 443–483.
22 P. Shu, Q. Peng, T. Luo, J. Ding, X. Gong, J. Zhou, Y. Yu, X. Qi and Z. Sun, *J. Mater. Chem. A*, 2024, **12**, 6515–6526.
23 W. Guo, X. Tan, S. Jia, S. Liu, X. Song, X. Ma, L. Wu, L. Zheng, X. Sun and B. Han, *CCS Chem.*, 2024, **6**, 1231–1239.
24 Y. Yang, S. Louisia, S. Yu, J. Jin, I. Roh, C. Chen, M. V. Fonseca Guzman, J. Feijóo, P.-C. Chen, H. Wang, C. J. Pollock, X. Huang, Y.-T. Shao, C. Wang, D. A. Muller, H. D. Abruña and P. Yang, *Nature*, 2023, **614**, 262–269.
25 G. Kresse and J. Furthmüller, *Phys. Rev. B*, 1996, **54**, 11169.
26 J. Hafner, *J. Comput. Chem.*, 2008, **29**, 2044–2078.
27 G. Kresse, *J. Non-Cryst. Solids*, 1995, **192–193**, 222–229.
28 G. Wang, L.-q. Peng, K. Li, L. Zhu, J. Zhou, N. Miao and Z. Sun, *Comput. Mater. Sci.*, 2021, **186**, 110064.
29 V. Wang, N. Xu, J.-C. Liu, G. Tang and W.-T. Geng, *Comput. Phys. Commun.*, 2021, **267**, 108033.
30 S. Grimme, J. Antony, S. Ehrlich and H. Krieg, *J. Chem. Phys.*, 2010, **132**, 154104.
31 L. Liu and H. Xiao, *J. Am. Chem. Soc.*, 2023, **145**, 14267–14275.
32 S. Steinberg and R. Dronskowski, *Crystals*, 2018, **8**, 225.
33 R. F. W. Bader, *Chem. Rev.*, 1991, **91**, 893–928.
34 G. Henkelman, A. Arnaldsson and H. Jónsson, *Comput. Mater. Sci.*, 2006, **36**, 354–360.
35 G. Henkelman, B. P. Uberuaga and H. Jónsson, *J. Chem. Phys.*, 2000, **113**, 9901–9904.

36 S. Nosé, *J. Chem. Phys.*, 1984, **81**, 511–519.
37 C. Laoire, S. Mukerjee, E. J. Plichta, M. A. Hendrickson and K. M. Abraham, *J. Electrochem. Soc.*, 2011, **158**, A302.
38 M. A. Rivas, T. P. Iglesias, S. M. Pereira and N. Banerji, *J. Chem. Thermodyn.*, 2006, **38**, 245–256.
39 J. Holoubek, H. Liu, Z. Wu, Y. Yin, X. Xing, G. Cai, S. Yu, H. Zhou, T. A. Pascal, Z. Chen and P. Liu, *Nat. Energy*, 2021, **6**, 303–313.
40 G. N. Greaves, A. L. Greer, R. S. Lakes and T. Rouxel, *Nat. Mater.*, 2011, **10**, 823–837.
41 Y. Zhu and X. Wu, *Prog. Mater. Sci.*, 2023, **131**, 101019.
42 B. Mortazavi, M. Silani, E. V. Podryabinkin, T. Rabczuk, X. Zhuang and A. V. Shapeev, *Adv. Mater.*, 2021, **33**, 2102807.
43 Q. Peng, K. Hu, B. Sa, J. Zhou, B. Wu, X. Hou and Z. Sun, *Nano Res.*, 2017, **10**, 3136–3150.
44 Y. Luo, Z. Ma, X. Xia, J. Zhong, P. Wu and Y. Huang, *ChemSusChem*, 2023, **16**, e202202209.
45 J. Cho, A. Medina, I. Saih, J. Il Choi, M. Drexler, W. A. Goddard Iii, F. M. Alamgir and S. S. Jang, *Angew. Chem., Int. Ed.*, 2024, **63**, e202320268.
46 P. Shu, X. Qi, Q. Peng, Y. Chen, X. Gong, Y. Zhang, F. Ouyang and Z. Sun, *Mol. Catal.*, 2023, **539**, 113036.
47 S. Jiao, X. Fu and H. Huang, *Adv. Funct. Mater.*, 2022, **32**, 2107651.
48 J. K. Nørskov, F. Abild-Pedersen, F. Studt and T. Bligaard, *Proc. Natl. Acad. Sci. U. S. A.*, 2011, **108**, 937–943.
49 Y. Hou, J. Wang, L. Liu, Y. Liu, S. Chou, D. Shi, H. Liu, Y. Wu, W. Zhang and J. Chen, *Adv. Funct. Mater.*, 2017, **27**, 1700564.
50 J. Hu, C. Yang and K. Guo, *J. Mater. Chem. A*, 2022, **10**, 14028–14040.
51 W. Zhao, Y. Yang, Q. Deng, Q. Dai, Z. Fang, X. Fu, W. Yan, L. Wu and Y. Zhou, *Adv. Funct. Mater.*, 2023, **33**, 2210037.
52 X. Sun, X. Mu, W. Zheng, L. Wang, S. Yang, C. Sheng, H. Pan, W. Li, C. H. Li, P. He and H. Zhou, *Nat. Commun.*, 2023, **14**, 536.
53 A. Ahmadiparidari, R. E. Warburton, L. Majidi, M. Asadi, A. Chamaani, J. R. Jokisaari, S. Rastegar, Z. Hemmat, B. Sayahpour, R. S. Assary, B. Narayanan, P. Abbasi, P. C. Redfern, A. Ngo, M. Vörös, J. Greeley, R. Klie, L. A. Curtiss and A. Salehi-Khojin, *Adv. Mater.*, 2019, **31**, 1902518.
54 Y. Liu, R. Mao, B. Chen, B. Lu, Z. Piao, Y. Song, G. Zhou and H. M. Cheng, *Mater. Today*, 2023, **63**, 120–136.
55 Y. Liu, S. Zhao, D. Wang, B. Chen, Z. Zhang, J. Sheng, X. Zhong, X. Zou, S. P. Jiang, G. Zhou and H. M. Cheng, *ACS Nano*, 2022, **16**, 1523–1532.
56 B. Chen, D. Wang, J. Tan, Y. Liu, M. Jiao, B. Liu, N. Zhao, X. Zou, G. Zhou and H.-M. Cheng, *J. Am. Chem. Soc.*, 2022, **144**, 3106–3116.
57 S. Li, Y. Dong, J. Zhou, Y. Liu, J. Wang, X. Gao, Y. Han, P. Qi and B. Wang, *Energy Environ. Sci.*, 2018, **11**, 1318–1325.
58 Z. Zhang, Q. Zhang, Y. Chen, J. Bao, X. Zhou, Z. Xie, J. Wei and Z. Zhou, *Angew. Chem., Int. Ed.*, 2015, **54**, 6550–6553.
59 Y. Qian, Y. Liu, Y. Zhao, X. Zhang and G. Yu, *EcoMat*, 2020, **2**, e12014.
60 Q. Jing, Z. Mei, X. Sheng, X. Zou, Q. Xu, L. Wang and H. Guo, *Adv. Funct. Mater.*, 2024, **34**, 2307002.
61 M. Gsell, P. Jakob and D. Menzel, *Science*, 1998, **280**, 717–720.
62 Y. Yan, J. Lin, K. Huang, X. Zheng, L. Qiao, S. Liu, J. Cao, S. C. Jun, Y. Yamauchi and J. Qi, *J. Am. Chem. Soc.*, 2023, **145**, 24218–24229.
63 C. Zhao, Y. Huang, B. Jiang, Z. Chen, X. Yu, X. Sun, H. Zhou, Y. Zhang and N. Zhang, *Adv. Energy Mater.*, 2024, **14**, 2302586.
64 Q. Peng, Z. Guo, B. Sa, J. Zhou and Z. Sun, *Int. J. Hydrogen Energy*, 2018, **43**, 15995–16004.
65 X.-P. Zhang, Y.-N. Li, Y.-Y. Sun and T. Zhang, *Angew. Chem., Int. Ed.*, 2019, **58**, 18394–18398.
66 Y. Chen, J. Li, B. Lu, Y. Liu, R. Mao, Y. Song, H. Li, X. Yu, Y. Gao, Q. Peng, X. Qi and G. Zhou, *Adv. Mater.*, 2024, DOI: **10.1002/adma.202406856**.
67 N. Lespes and J.-S. Filhol, *J. Chem. Theory Comput.*, 2015, **11**, 3375–3382.
68 L. Miao, W. Jia, X. Cao and L. Jiao, *Chem. Soc. Rev.*, 2024, **53**, 2771–2807.
69 X. Hu, S. Chen, L. Chen, Y. Tian, S. Yao, Z. Lu, X. Zhang and Z. Zhou, *J. Am. Chem. Soc.*, 2022, **144**, 18144–18152.